
ENTROPY-MCMC: SAMPLING FROM FLAT BASINS WITH EASE

Bolian Li, Ruqi Zhang

Department of Computer Science, Purdue University, USA
 {li4468, ruqiz}@purdue.edu

ABSTRACT

Bayesian deep learning counts on the quality of posterior distribution estimation. However, the posterior of deep neural networks is highly multi-modal in nature, with local modes exhibiting varying generalization performance. Given a practical budget, sampling from the original posterior can lead to suboptimal performance, as some samples may become trapped in “bad” modes and suffer from overfitting. Leveraging the observation that “good” modes with low generalization error often reside in flat basins of the energy landscape, we propose to bias sampling on the posterior toward these flat regions. Specifically, we introduce an auxiliary guiding variable, the stationary distribution of which resembles a smoothed posterior free from sharp modes, to lead the MCMC sampler to flat basins. By integrating this guiding variable with the model parameter, we create a simple joint distribution that enables efficient sampling with minimal computational overhead. We prove the convergence of our method and further show that it converges faster than several existing flatness-aware methods in the strongly convex setting. Empirical results demonstrate that our method can successfully sample from flat basins of the posterior, and outperforms all compared baselines on multiple benchmarks including classification, calibration, and out-of-distribution detection.

1 INTRODUCTION

The effectiveness of Bayesian neural networks relies heavily on the quality of posterior distribution estimation. However, achieving an accurate estimation of the full posterior is extremely difficult due to its high-dimensional and highly multi-modal nature (Zhang et al., 2020b; Izmailov et al., 2021). Moreover, the numerous modes in the energy landscape typically exhibit varying generalization performance. Flat modes often show superior accuracy and robustness, whereas sharp modes tend to have high generalization errors (Hochreiter & Schmidhuber, 1997; Keskar et al., 2017; Bahri et al., 2022). This connection between the geometry of energy landscape and generalization has spurred many works in optimization, ranging from theoretical understanding (Neysshabur et al., 2017; Dinh et al., 2017; Dziugaite & Roy, 2018; Jiang et al., 2019a) to new optimization algorithms (Mobahi, 2016; Izmailov et al., 2018; Chaudhari et al., 2019; Foret et al., 2020).

However, most of the existing Bayesian methods are not aware of the flatness in the energy landscape during posterior inference (Welling & Teh, 2011; Chen et al., 2014; Ma et al., 2015; Zhang et al., 2020b). Their inference strategies are usually energy-oriented and could not distinguish between flat and sharp modes that have the same energy values. This limitation can significantly undermine their generalization performance, particularly in practical situations where capturing the full posterior is challenging. In light of this, we contend that prioritizing the capture of flat modes is essential when conducting posterior inference for Bayesian neural networks. This is advantageous for improved generalization as justified by previous works (Hochreiter & Schmidhuber, 1997; Keskar et al., 2017; Bahri et al., 2022). It can further be rationalized from a Bayesian marginalization perspective: within the flat basin, each model configuration occupies a substantial volume and contributes significantly to a more precise estimation of the predictive distribution (Bishop, 2006). Moreover, existing flatness-aware methods often rely on a single solution to represent the entire flat basin (Chaudhari et al., 2019; Foret et al., 2020), ignoring the fact that the flat basin contains many high-performing models. Therefore, Bayesian marginalization can potentially offer significant improvements over flatness-aware optimization by sampling from the flat basins (Wilson, 2020; Huang et al., 2020).

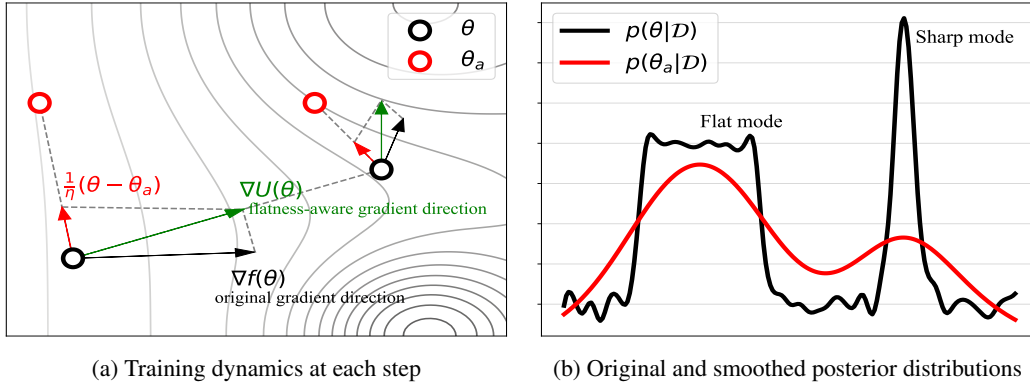


Figure 1: Illustration of Entropy-MCMC. (a) shows how the guiding variable θ_a pulls θ toward flat basins; (b) shows two posterior distributions, where $p(\theta_a|\mathcal{D})$ is a smoothed distribution transformed from $p(\theta|\mathcal{D})$, and only keeps flat modes. Entropy-MCMC prioritizes flat modes by leveraging the guiding variable θ_a from the smoothed posterior as a form of regularization.

Prioritizing flat basins during posterior inference poses an additional challenge to Bayesian inference. Even for a single point estimation, explicitly biasing toward the flat basins will introduce substantial computational overhead, inducing nested loops (Chaudhari et al., 2019; Dziugaite & Roy, 2018), doubled gradients calculation (Foret et al., 2020; Möllenhoff & Khan, 2022) or min-max problems (Foret et al., 2020). The efficiency problem needs to be addressed before any flatness-aware Bayesian method becomes practical for deep neural networks.

In this paper, we propose an efficient sampling algorithm to explicitly prioritize flat basins in the energy landscape of deep neural networks. Specifically, we introduce an auxiliary guiding variable θ_a into the Markov chain to pull the model parameter θ toward flat basins at each updating step (Fig. 1a). θ_a is sampled from a smoothed posterior distribution which eliminates sharp modes based on local entropy (Baldassi et al., 2016) (Fig. 1b). Our method enjoys a simple joint distribution of θ and θ_a , and the computational overhead is similar to Stochastic gradient Langevin dynamics (SGLD) (Welling & Teh, 2011). Theoretically, we prove that our method is guaranteed to converge faster than some common flatness-aware methods (Chaudhari et al., 2019; Dziugaite & Roy, 2018) in the strongly convex setting. Empirically, we demonstrate that our method successfully finds flat basins efficiently across multiple tasks. Our main contributions are summarized as follows:

- We propose Entropy-MCMC (EMCMC) for sampling from flat basins in the energy landscape of deep neural networks. EMCMC utilizes an auxiliary guiding variable and a simple joint distribution to efficiently steer the model toward flat basins.
- We prove the convergence of EMCMC and further show that it converges faster than several existing flatness-aware methods in the strongly convex setting.
- We provide extensive experimental results to demonstrate the advantages of EMCMC in sampling from flat basins. EMCMC outperforms all compared baselines on classification, calibration, and out-of-distribution detection with comparable overhead akin to SGLD.

2 RELATED WORKS

Flatness-aware Optimization. The concept of flatness in the energy landscape was first studied by Hochreiter & Schmidhuber (1994), and its connection with generalization was then empirically discussed by Keskar et al. (2017); Dinh et al. (2017); Jiang et al. (2019b). In order to pursue flatness for better generalization, Entropy-SGD (Chaudhari et al., 2019) introduced local entropy to consider the averaged loss of a region, SAM (Foret et al., 2020) developed a new optimizer to minimize the worst-case near the current model, bSAM (Möllenhoff & Khan, 2022) further improved SAM with a Bayes optimal convex lower bound, LPF (Bisla et al., 2022) introduced low-pass filter to actively search flat basins, and SWA (Izmailov et al., 2018) found that averaging weights along

the trajectory of SGD training can also find flatter modes. Our Entropy-MCMC follows the local entropy measurement and collects more than a single point to fully exploit the flat basins.

MCMC on Deep Neural Networks. Markov chain Monte Carlo is a class of general and practical sampling algorithms (Andrieu et al., 2003), which has been applied to infer Bayesian neural network posteriors (Neal, 2012). SGMCMC (Welling & Teh, 2011; Ma et al., 2015) methods use the mini-batching technique to adapt MCMC to deep neural networks. SGHMC (Chen et al., 2014) exploited the second-order Langevin dynamics to calibrate the stochastic estimates of HMC gradients. cSGMCMC (Zhang et al., 2020b) further improves sampling efficiency by leveraging a cyclical step size schedule. Symmetric Split HMC (Cobb & Jalaian, 2021) developed a way to apply HMC to deep neural networks without stochastic gradients. Our Entropy-MCMC builds upon the SGMCMC framework and is designed to favor the flat basins in the energy landscape during sampling.

3 PRELIMINARIES

Flatness-aware Optimization. One common flatness-aware optimization technique is to use the concept of *local entropy*, which measures the geometric properties of the energy landscape (Baldassi et al., 2016; Chaudhari et al., 2019). The local entropy is computed by:

$$\mathcal{F}(\boldsymbol{\theta}; \eta) = \log \int_{\Theta} \exp \left\{ -f(\boldsymbol{\theta}') - \frac{1}{2\eta} \|\boldsymbol{\theta} - \boldsymbol{\theta}'\|^2 \right\} d\boldsymbol{\theta}', \quad (1)$$

where $f(\cdot)$ is the loss function and η is a scalar. The local entropy of a point $\boldsymbol{\theta}$ is determined by its neighbors weighted by their distances, which considers the volume of local modes. Previous optimization methods minimize $-\mathcal{F}(\boldsymbol{\theta}; \eta)$ to find the flat minimum.

SGMCMC. Given a dataset \mathcal{D} , a neural network with the parameter $\boldsymbol{\theta} \in \mathbb{R}^d$ and a prior distribution $p(\boldsymbol{\theta})$, we can use Markov chain Monte Carlo (MCMC) to sample from the posterior $p(\boldsymbol{\theta}|\mathcal{D}) \propto \exp(-U(\boldsymbol{\theta}))$, where the energy function is $U(\boldsymbol{\theta}) = -\sum_{x \in \mathcal{D}} \log p(x|\boldsymbol{\theta}) - \log p(\boldsymbol{\theta})$. However, the computational cost for MCMC with large-scale data is too high to be practical. SGMCMC tackles this problem by stochastic gradient ∇U_{Ξ} based on a subset of data $\Xi \subseteq \mathcal{D}$. We use Stochastic Gradient Langevin Dynamics (SGLD) (Welling & Teh, 2011) in the paper as the backbone MCMC algorithm, which has the following updating rule:

$$\boldsymbol{\theta} \leftarrow \boldsymbol{\theta} - \alpha \nabla_{\boldsymbol{\theta}} U_{\Xi}(\boldsymbol{\theta}) + \sqrt{2\alpha} \cdot \boldsymbol{\epsilon}, \quad (2)$$

where α is the step size and $\boldsymbol{\epsilon}$ is standard Gaussian noise. Our method can also be implemented by other SGMCMC methods. During testing, Bayesian marginalization is performed to make predictions based on the sample set collected during sampling $\mathcal{S} = \{\boldsymbol{\theta}_j\}_{j=1}^M$ and the predictive distribution is obtained by $p(y|\mathbf{x}, \mathcal{D}) = \int p(y|\mathbf{x}, \boldsymbol{\theta}) p(\boldsymbol{\theta}|\mathcal{D}) d\boldsymbol{\theta} \approx \sum_{\boldsymbol{\theta} \in \mathcal{S}} p(y|\mathbf{x}, \boldsymbol{\theta})$.

4 ENTROPY-MCMC

In this section, we present the Entropy-MCMC algorithm. We introduce the guiding variable $\boldsymbol{\theta}_a$ obtained from the local entropy in section 4.1 and discuss the sampling strategy in section 4.2.

4.1 FROM LOCAL ENTROPY TO FLAT POSTERIOR

While flat basins in the energy landscape have been shown to be of good generalization (Hochreiter & Schmidhuber, 1997; Keskar et al., 2017; Bahri et al., 2022), finding such regions is still challenging due to the highly multi-modal nature of the DNN energy landscape. The updating direction of the model typically needs extra force to mitigate the risk of converging to sharp modes (Chaudhari et al., 2019; Foret et al., 2020). To bias sampling to flat basins, we look into the local entropy (Eq. 1), which can eliminate the sharp modes in the energy landscape (Chaudhari et al., 2019).

We begin by the original posterior distribution $p(\boldsymbol{\theta}|\mathcal{D}) \propto \exp(-f(\boldsymbol{\theta})) = \exp\{\log p(\mathcal{D}|\boldsymbol{\theta}) + \log p(\boldsymbol{\theta})\}$, which contains both sharp and flat modes. By replacing the original loss function with local entropy, we obtain a smoothed posterior distribution in terms of a new variable $\boldsymbol{\theta}_a$:

$$p(\boldsymbol{\theta}_a|\mathcal{D}) \propto \exp \mathcal{F}(\boldsymbol{\theta}_a; \eta) = \int_{\Theta} \exp \left\{ -f(\boldsymbol{\theta}) - \frac{1}{2\eta} \|\boldsymbol{\theta} - \boldsymbol{\theta}_a\|^2 \right\} d\boldsymbol{\theta}. \quad (3)$$

The effect of local entropy on this new posterior is visualized in Fig. 1b. The new posterior measures both the depth and flatness of the mode in $p(\boldsymbol{\theta}|\mathcal{D})$ by considering surrounding energy values. Thereby, $p(\boldsymbol{\theta}_a|\mathcal{D})$ is expected to primarily capture flat modes in the energy landscape, which can be used as the desired external force to revise the updating directions of the model parameter $\boldsymbol{\theta}$.

However, the complex integral in Eq. 3 requires marginalization on the model parameter $\boldsymbol{\theta}$, which poses a non-trivial challenge. Previous works using local entropy usually adopt an inner Markov chain with Monte Carlo (MC) approximation (Chaudhari et al., 2019; Dziugaite & Roy, 2018), which sacrifices the accuracy of local entropy computation and induces computationally expensive nested loops in training. We tackle this challenge in a simple yet principled manner, eliminating the need for nested loops or approximation. This is achieved by *coupling* $\boldsymbol{\theta} \sim p(\boldsymbol{\theta}|\mathcal{D})$ and $\boldsymbol{\theta}_a \sim p(\boldsymbol{\theta}_a|\mathcal{D})$ into a joint posterior distribution, which enjoys a simple form, as discussed in Lemma 1.

Lemma 1. Assume $\tilde{\boldsymbol{\theta}} = [\boldsymbol{\theta}^T, \boldsymbol{\theta}_a^T]^T \in \mathbb{R}^{2d}$ and $\tilde{\boldsymbol{\theta}}$ has the following distribution:

$$p(\tilde{\boldsymbol{\theta}}|\mathcal{D}) = p(\boldsymbol{\theta}, \boldsymbol{\theta}_a|\mathcal{D}) \propto \exp \left\{ -f(\boldsymbol{\theta}) - \frac{1}{2\eta} \|\boldsymbol{\theta} - \boldsymbol{\theta}_a\|^2 \right\}. \quad (4)$$

Then the marginal distributions of $\boldsymbol{\theta}$ and $\boldsymbol{\theta}_a$ are the original posterior $p(\boldsymbol{\theta}|\mathcal{D})$ and $p(\boldsymbol{\theta}_a|\mathcal{D})$ (Eq. 3).

This joint posterior offers three key advantages: i) by coupling $\boldsymbol{\theta}$ and $\boldsymbol{\theta}_a$, we avoid the intricate integral computation, and thus remove the requirement of expensive nested training loops and mitigate the MC approximation error; ii) the joint posterior turns out to be surprisingly simple, making it easy to sample from both empirically and theoretically (details discussed in Sections 4.2 and 5); iii) after coupling, $\boldsymbol{\theta}_a$ provides additional paths for $\boldsymbol{\theta}$ to traverse, making $\boldsymbol{\theta}$ reach flat modes efficiently.

4.2 SAMPLING FROM FLAT BASINS

We discuss how to sample from the joint posterior distribution (Eq. 4) in this section. We adopt SGLD (Welling & Teh, 2011), a simple stochastic gradient MCMC algorithm that is suitable for deep neural networks, as the backbone of EMCMC sampling. More advanced MCMC algorithms can also be combined with our method. The energy function of the joint parameter variable $\tilde{\boldsymbol{\theta}}$ is $U(\tilde{\boldsymbol{\theta}}) = f(\boldsymbol{\theta}) + \frac{1}{2\eta} \|\boldsymbol{\theta} - \boldsymbol{\theta}_a\|^2$, and thus its gradients is given by:

$$\nabla_{\tilde{\boldsymbol{\theta}}} U(\tilde{\boldsymbol{\theta}}) = \begin{bmatrix} \nabla_{\boldsymbol{\theta}} U(\tilde{\boldsymbol{\theta}}) \\ \nabla_{\boldsymbol{\theta}_a} U(\tilde{\boldsymbol{\theta}}) \end{bmatrix} = \begin{bmatrix} \nabla_{\boldsymbol{\theta}} f(\boldsymbol{\theta}) + \frac{1}{\eta}(\boldsymbol{\theta} - \boldsymbol{\theta}_a) \\ \frac{1}{\eta}(\boldsymbol{\theta}_a - \boldsymbol{\theta}) \end{bmatrix}. \quad (5)$$

For the model parameter $\boldsymbol{\theta}$, the original gradient direction $\nabla_{\boldsymbol{\theta}} f(\boldsymbol{\theta})$ is revised by $\frac{1}{\eta}(\boldsymbol{\theta} - \boldsymbol{\theta}_a)$ to get the flatness-aware gradient direction $\nabla_{\boldsymbol{\theta}} U(\tilde{\boldsymbol{\theta}})$, as visualized in Fig. 1a. Importantly, the practical implementation does not require computing $\nabla_{\boldsymbol{\theta}_a} U(\tilde{\boldsymbol{\theta}})$ through back-propagation, as we can utilize the analytical expression presented in Eq. 5. Therefore, despite $\tilde{\boldsymbol{\theta}}$ being in a $2d$ dimension, our cost of gradient computation is essentially the *same* as d -dimensional models (e.g., standard SGLD).

With the form of the gradients in Eq. 5, the training procedure of EMCMC is straightforward using the SGLD updating rule in Eq. 2. The details are summarized in Algorithm 1. At testing stage, the collected samples \mathcal{S} are used to approximate the predictive distribution $p(y|\mathbf{x}, \mathcal{D}) \approx \sum_{\boldsymbol{\theta}_s \in \mathcal{S}} p(y|\mathbf{x}, \boldsymbol{\theta}_s)$. Our choice of sampling from the joint posterior distribution using SGLD, rather than a Gibbs-like approach (Gelfand, 2000), is motivated by SGLD’s ability to simultaneously update both $\boldsymbol{\theta}$ and $\boldsymbol{\theta}_a$, which is more efficient than alternative updating (see Appendix A for a detailed discussion). For the sample set \mathcal{S} , we collect both $\boldsymbol{\theta}$ and $\boldsymbol{\theta}_a$ after the burn-in period in order to obtain more high-quality and diverse samples in a given time budget (see Appendix C.3 for details).

In summary, thanks to EMCMC’s simple joint distribution, conducting sampling in EMCMC is straightforward, and its computational cost is comparable to that of standard SGLD. Despite its algorithmic simplicity and computational efficiency, EMCMC is guaranteed to bias sampling to flat basins and obtain samples with enhanced generalization and robustness.

5 THEORETICAL ANALYSIS

In this section, we provide a theoretical analysis on the convergence rate of Entropy-MCMC and compare it with previous local-entropy-based methods including Entropy-SGD (Chaudhari et al.,

Algorithm 1: Entropy-MCMC

Inputs: The model parameter $\theta \in \Theta$, guiding variable $\theta_a \in \Theta$, and dataset $\mathcal{D} = \{(\mathbf{x}_i, y_i)\}_{i=1}^N$;

Results: Collected samples $\mathcal{S} \subset \Theta$;

```
 $\theta_a \leftarrow \theta, \mathcal{S} \leftarrow \emptyset;$  /* Initialize */  
for each iteration do  
   $\Xi \leftarrow$  A mini-batch sampled from  $\mathcal{D}$ ;  
   $U_\Xi \leftarrow -\log p(\Xi|\theta) - \log p(\theta) + \frac{1}{2\eta}\|\theta - \theta_a\|^2;$   
   $\theta \leftarrow \theta - \alpha \nabla_\theta U_\Xi + \sqrt{2\alpha} \cdot \epsilon_1;$  /*  $\epsilon_1, \epsilon_2 \sim \mathcal{N}(\mathbf{0}, \mathbf{I})$  */  
   $\theta_a \leftarrow \theta_a - \alpha \nabla_{\theta_a} U_\Xi + \sqrt{2\alpha} \cdot \epsilon_2;$   
  
  if after burn-in then  
     $\mathcal{S} \leftarrow \mathcal{S} \cup \{\theta, \theta_a\};$  /* Collect samples */  
  end  
end
```

2019) and Entropy-SGLD (Dziugaite & Roy, 2018) (used as a theoretical tool in the literature rather than a practical algorithm). We leverage the 2-Wasserstein distance bounds of SGLD, which assumes the target distribution to be smooth and strongly log-concave (Dalalyan & Karagulyan, 2019). While the target distribution in this case is unimodal, it still reveals the superior convergence rate of EMCMC compared with existing flatness-aware methods. We leave the theoretical analysis on non-log-concave distributions for future work. Specifically, we have the following assumptions for the loss function $f(\cdot)$ and stochastic gradients:

Assumption 1. The loss function $f(\theta)$ in the original posterior distribution $\pi = p(\theta|\mathcal{D}) \propto \exp(-f(\theta))$ is M -smooth and m -strongly convex (i.e., $m\mathbf{I} \preceq \nabla^2 f(\theta') \preceq M\mathbf{I}$).

Assumption 2. The variance of stochastic gradients is bounded by $\mathbb{E}[\|\nabla f(\theta) - \nabla f_\Xi(\theta)\|^2] \leq \sigma^2$ for some constant $\sigma > 0$.

To establish the convergence analysis for EMCMC, we first observe that the smoothness and convexity properties of the joint posterior distribution $\pi_{\text{joint}}(\theta, \theta_a) = p(\theta, \theta_a|\mathcal{D})$ in Eq. 4 is the same as the original posterior $p(\theta|\mathcal{D})$, which is formally stated in Lemma 2.

Lemma 2. If Assumption 1 holds and $m \leq 1/\eta \leq M$, then the energy function in the joint posterior distribution $\pi_{\text{joint}}(\theta, \theta_a) = p(\theta, \theta_a|\mathcal{D})$ is also M -smooth and m -strongly convex.

With the convergence bound of SGLD established by Dalalyan & Karagulyan (2019), we derive the convergence bound for EMCMC in Theorem 1.

Theorem 1. Under Assumptions 1 and 2, let μ_0 be the initial distribution and μ_K be the distribution obtained by EMCMC after K iterations. If $m \leq 1/\eta \leq M$ and the step size $\alpha \leq 2/(m + M)$, the 2-Wasserstein distance between μ_K and π_{joint} will have the following upper bound:

$$\mathcal{W}_2(\mu_K, \pi_{\text{joint}}) \leq (1 - \alpha m)^K \cdot \mathcal{W}_2(\mu_0, \pi) + 1.65(M/m)(2\alpha d)^{1/2} + \frac{\sigma^2(2\alpha d)^{1/2}}{1.65M + \sigma\sqrt{m}}. \quad (6)$$

Comparing Theorem 1 with the convergence bound of SGLD obtained by Dalalyan & Karagulyan (2019), the only difference is the doubling of the dimension, from d to $2d$. Theorem 1 implies that the convergence rate of EMCMC will have at most a minor slowdown by a constant factor compared to SGLD while ensuring sampling from flat basins.

In contrast, previous local-entropy-based methods often substantially slow down the convergence in order to bias toward flat basins. For example, consider Entropy-SGD (Chaudhari et al., 2019) which minimizes a flattened loss function $f_{\text{flat}}(\theta) = -\mathcal{F}(\theta; \eta) = -\log \int_{\Theta} \exp\left\{-f(\theta') - \frac{1}{2\eta}\|\theta - \theta'\|^2\right\} d\theta'$. We discuss the convergence bound of Entropy-SGD in Theorem 2, which shows how the presence of the integral (and the nested Markov chain induced by it) slows down the convergence.

Theorem 2. Consider running Entropy-SGD to minimize the flattened loss function $f_{\text{flat}}(\theta)$ under Assumptions 1 and 2. Assume the inner Markov chain runs L iterations and the 2-Wasserstein

distance between the initial and target distributions is always bounded by κ . Let f_{flat}^* represent the global minimum value of $f_{\text{flat}}(\boldsymbol{\theta})$ and $E_t := \mathbb{E}f_{\text{flat}}(\boldsymbol{\theta}_t) - f_{\text{flat}}^*$. If the step size $\alpha \leq 2/(m + M)$, then we have the following upper bound:

$$E_K \leq \left(1 - \frac{\alpha m}{1 + \eta M}\right)^K \cdot E_0 + \frac{A(1 + \eta M)}{2m}, \quad (7)$$

where $A^2 = (1 - \alpha m)^L \cdot \kappa + 1.65 \left(\frac{M+1/\eta}{m+1/\eta}\right) (\alpha d)^{1/2} + \frac{\sigma^2(\alpha d)^{1/2}}{1.65(M+1/\eta) + \sigma\sqrt{m+1/\eta}}$.

Another example is Entropy-SGLD (Dziugaite & Roy, 2018), a theoretical tool established to analyze Entropy-SGD. Its main distinction with Entropy-SGD is the SGLD updating instead of SGD updating in the outer loop. The convergence bound for Entropy-SGLD is established in Theorem 3.

Theorem 3. Consider running Entropy-SGLD to sample from $\pi_{\text{flat}}(\boldsymbol{\theta}) \propto \exp \mathcal{F}(\boldsymbol{\theta}; \eta)$ under Assumptions 1 and 2. Assume the inner Markov chain runs L iterations and the 2-Wasserstein distance between initial and target distributions is always bounded by κ . Let ν_0 be the initial distribution and ν_K be the distribution obtained by Entropy-SGLD after K iterations. If the step size $\alpha \leq 2/(m + M)$, then:

$$\mathcal{W}_2(\nu_K, \pi_{\text{flat}}) \leq (1 - \alpha m)^K \cdot \mathcal{W}_2(\nu_0, \pi_{\text{flat}}) + 1.65 \left(\frac{1 + \eta M}{1 + \eta m}\right) (M/m)(\alpha d)^{1/2} + \frac{A(1 + \eta M)}{m}, \quad (8)$$

where $A^2 = (1 - \alpha m)^L \cdot \kappa + 1.65 \left(\frac{M+1/\eta}{m+1/\eta}\right) (\alpha d)^{1/2} + \frac{\sigma^2(\alpha d)^{1/2}}{1.65(M+1/\eta) + \sigma\sqrt{m+1/\eta}}$.

Comparing Theorem 1, 2 and 3, we observe that the convergence rates of Entropy-SGD and Entropy-SGLD algorithms are significantly hindered due to the presence of the nested Markov chains, which induces a large and complicated error term A . Since σ and α are typically very small, the third term in Theorem 1 will be much smaller than both the third term in Theorem 3 and the second term in Theorem 2. To summarize, we prove that the convergence rate of Entropy-MCMC is notably better than that of Entropy-SGD and Entropy-SGLD in the strongly convex setting.

6 EXPERIMENTS

We conduct comprehensive experiments to show the superiority of EMCMC. Section 6.1 and 6.3 demonstrate that EMCMC can successfully sample from flat basins. Section 6.2 verifies the fast convergence of EMCMC. Section 6.4 and 6.5 demonstrate the outstanding performance of EMCMC on multiple benchmarks. Following Zhang et al. (2020b), we adopt a cyclical step size schedule for all sampling methods. For more implementation details, please refer to Appendix C.

6.1 SYNTHETIC EXAMPLES

To demonstrate EMCMC’s capability to sample from flat basins, we construct a two-mode energy landscape $\frac{1}{2}\mathcal{N}([-2, -1]^T, 0.5\mathbf{I}) + \frac{1}{2}\mathcal{N}([2, 1]^T, \mathbf{I})$ containing a sharp and a flat mode. To make the case challenging, we set the initial point at $(-0.2, -0.2)$, the ridge of the two modes, which has no strong preference for either mode. Fig. 2 shows that the proposed EMCMC finds the flat basin while SGD and SGLD still prefer the sharp mode due to the slightly larger gradients coming from the sharp mode. From Fig. 2(c)&(d), we see that the samples of $\boldsymbol{\theta}_a$ are always around the flat mode, showing its ability to eliminate the sharp mode. Although $\boldsymbol{\theta}$ visits the sharp mode in the first few iterations, it subsequently inclines toward the flat mode, illustrating the influence of gradient revision by the guiding variable $\boldsymbol{\theta}_a$. It is noteworthy that the result of EMCMC is essentially *independent* of initialization with appropriate values of η , since the guiding variable $\boldsymbol{\theta}_a$ will always steer $\boldsymbol{\theta}$ to the flat mode. We show the results for different initialization in Appendix D.

6.2 LOGISTIC REGRESSION

To verify the theoretical results on convergence rates in Section 5, we conduct logistic regression on MNIST (LeCun, 1998) to compare EMCMC with Entropy-SGD Chaudhari et al. (2019), SGLD (Welling & Teh, 2011) and Entropy-SGLD (Dziugaite & Roy, 2018). We follow Maclaurin

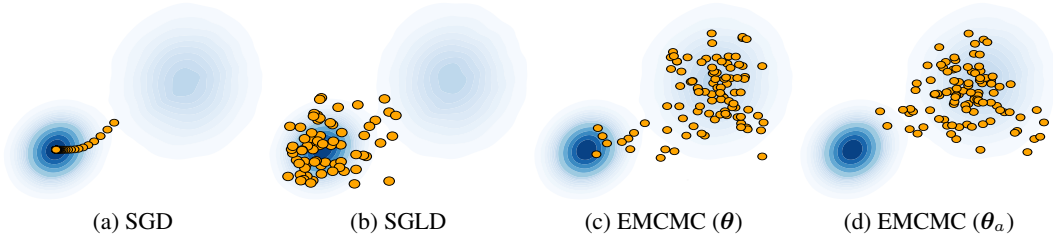


Figure 2: Sampling trajectories on a synthetic energy landscape with sharp (lower left) and flat (top right) modes. The initial point is located at the ridge of two modes. EMCMC successfully biases toward the flat mode whereas SGD and SGLD are trapped in the sharp mode.

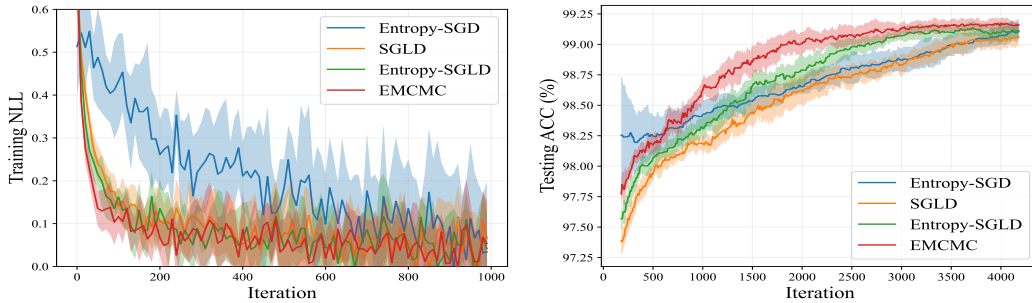


Figure 3: Logistic regression on MNIST in terms of training NLL and testing accuracy (repeated 10 times). EMCMC converges faster than others, which is consistent with our theoretical analysis.

& Adams (2015) and Zhang et al. (2020a) to use a subset containing 7s and 9s and the resulting posterior is strongly log-concave, satisfying the assumptions in Section 5. Fig. 3 shows that EMCMC converges faster than Entropy-SG(L)D, demonstrating the advantage of using a simple joint distribution without the need for nested loops or MC approximation, which verifies Theorems 1& 2& 3. Besides, while EMCMC and SGLD share similar convergence rates, EMCMC achieves better generalization as shown by its higher test accuracy. This suggests that EMCMC is potentially beneficial in unimodal distributions under limited budgets due to finding samples with high volumes.

6.3 FLATNESS ANALYSIS ON DEEP NEURAL NETWORKS

We perform flatness analysis with ResNet18 (He et al., 2016) on CIFAR100 (Krizhevsky, 2009). We use the last sample of SGD, SGLD, and EMCMC (averaged result from θ and θ_α) respectively, and each experiment is repeated 3 times to report the averaged scores.

Eigenspectrum of Hessian. The Hessian matrix of the model parameter measures the second-order gradients of a local mode on the energy landscape. Smaller eigenvalues of Hessian indicate a flatter local geometry (Chaudhari et al., 2019; Foret et al., 2020). Since computing the exact Hessian of deep neural networks is extremely costly, we use the diagonal Fisher information matrix (Wasserman, 2004) to approximate its eigenspectrum:

$$[\lambda_1, \dots, \lambda_d]^T \approx \text{diag}(\mathcal{I}(\theta)) = \mathbb{E} \left[(\nabla U - \mathbb{E} \nabla U)^2 \right], \quad (9)$$

where $\lambda_1, \dots, \lambda_d$ are eigenvalues of the Hessian. Fig. 4 shows the eigenspectra of local modes discovered by different algorithms. The eigenvalues of EMCMC are much smaller compared with SGD and SGLD, indicating that the local geometry of EMCMC samples is flatter. The eigenspectrum comparison verifies the effectiveness of EMCMC to find and sample from flat basins.

Parameter Space Interpolation. Another way to measure the flatness of local modes is directly interpolating their neighborhood in the parameter space (Izmailov et al., 2018). Local modes located

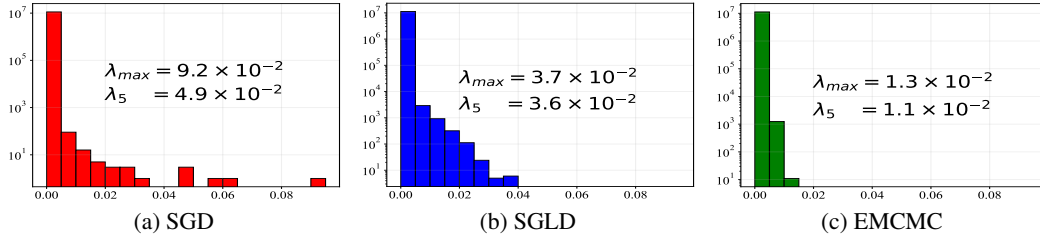


Figure 4: Eigenspectrum of Hessian matrices of ResNet18 on CIFAR100. x -axis: eigenvalue, y -axis: frequency. A nearly all-zero eigenspectrum indicates a local mode that is flat in all directions. EMCMC successfully finds such flat modes with significantly smaller eigenvalues.

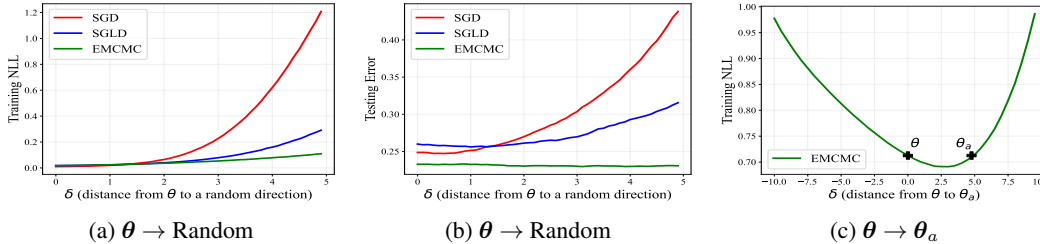


Figure 5: Parameter space interpolation of ResNet18 on CIFAR100. Exploring the neighborhood of local modes from θ to (a)-(b): a random direction in the parameter space, and (c): θ_a . (a) and (b) show that EMCMC has the lowest and the most flat NLL and error curves. (c) shows that θ and θ_a converge to the same flat mode while maintaining diversity.

in flat basins are expected to have larger widths and better generalization performance (Keskar et al., 2017; Chaudhari et al., 2019). The interpolation begins at θ and ends at θ_ϵ (a random point near θ or $\theta_\epsilon = \theta_a$). The interpolated point θ_δ is computed by:

$$\theta_\delta = (1 - \delta/\|\theta - \theta_\epsilon\|)\theta + (\delta/\|\theta - \theta_\epsilon\|)\theta_\epsilon, \quad (10)$$

where δ is the Euclidean distance from θ to θ_δ . Fig. 5a and 5b show the training NLL and testing error respectively. The neighborhood of EMCMC maintains consistently lower NLL and errors compared with SGD and SGLD, demonstrating that EMCMC samples are from flatter modes. Furthermore, Fig. 5c visualizes the interpolation between θ and θ_a , revealing that both variables essentially converge to the same flat mode while maintaining diversity. This justifies the benefit of collecting both of them as samples to obtain a diverse set of high-performing samples.

6.4 IMAGE CLASSIFICATION

We conduct classification experiments on CIFAR (Krizhevsky, 2009), corrupted CIFAR (Hendrycks & Dietterich, 2019b) and ImageNet (Deng et al., 2009), to compare EMCMC with both flatness-aware optimization methods (Entropy-SGD (Chaudhari et al., 2019), SAM (Foret et al., 2020) and bSAM (Möllenhoff & Khan, 2022)) and MCMC methods (SGLD (Welling & Teh, 2011) and Entropy-SGLD (Dziugaite & Roy, 2018)). We use ResNet18 and ResNet50 (He et al., 2016) for CIFAR and ImageNet respectively. All sampling algorithms collect a total of 16 samples for Bayesian marginalization, and all entries are repeated 3 times to report the mean \pm std. Table 1 shows the results on the 3 datasets, in which EMCMC significantly outperforms all baselines. The classification results strongly suggest that by sampling from flat basins, Bayesian neural networks can achieve outstanding performance and EMCMC is an effective and efficient method to do so.

The results for corrupted CIFAR (Hendrycks & Dietterich, 2019a) are shown in Table 1b to show the robustness of EMCMC against multiple types of noises. The results are averaged over all noise types, and the severity level refers to the strength of noise added to the original data. EMCMC consistently outperforms all compared baselines across all severity levels, indicating that samples from flat basins are more robust to noise. The results for individual noise types are shown in Appendix D.

Table 1: Classification results on (a) CIFAR10/100, (b) corrupted CIFAR and (c) ImageNet, measured by NLL and accuracy. EMCMC outperforms all compared baselines.

(a) CIFAR10 and CIFAR100									
Method	CIFAR10					CIFAR100			
	ACC (%) \uparrow	NLL \downarrow				ACC (%) \uparrow	NLL \downarrow		
SGD	94.87 \pm 0.04	0.205 \pm 0.015				76.49 \pm 0.27	0.935 \pm 0.021		
Entropy-SGD	95.11 \pm 0.09	0.184 \pm 0.020				77.45 \pm 0.03	0.895 \pm 0.009		
SAM	95.25 \pm 0.12	0.166 \pm 0.005				78.41 \pm 0.22	0.876 \pm 0.007		
bSAM	95.53 \pm 0.09	0.165 \pm 0.002				78.92 \pm 0.25	0.870 \pm 0.005		
SGLD	95.47 \pm 0.11	0.167 \pm 0.011				78.79 \pm 0.35	0.854 \pm 0.031		
Entropy-SGLD	94.46 \pm 0.24	0.194 \pm 0.020				77.98 \pm 0.39	0.897 \pm 0.027		
EMCMC	95.69 \pm 0.06	0.162 \pm 0.002				79.16 \pm 0.07	0.840 \pm 0.004		

(b) Corrupted CIFAR (ACC (%) \uparrow)						(c) ImageNet			
Severity	1	2	3	4	5	Metric	NLL \downarrow	Top-1 (%) \uparrow	Top-5 (%) \uparrow
SGD	88.43	82.43	76.20	67.93	55.81	SGD	0.960	76.046	92.776
SGLD	88.61	82.46	76.49	69.19	56.98	SGLD	0.921	76.676	93.174
EMCMC	88.87	83.27	77.44	70.31	58.17	EMCMC	0.895	77.096	93.424

Table 2: OOD detection on CIFAR-SVHN. The predictive uncertainty quantified by EMCMC is the best among the compared algorithms.

Method	CIFAR10-SVHN					CIFAR100-SVHN			
	AUC (%) \uparrow	ECE (%) \downarrow				AUC (%) \uparrow	ECE (%) \downarrow		
SGD	96.67 \pm 0.98	18.09 \pm 6.42				74.85 \pm 1.69	14.74 \pm 2.43		
Entropy-SGD	98.17 \pm 0.73	6.95 \pm 4.22				78.89 \pm 2.97	9.30 \pm 3.50		
SAM	98.01 \pm 0.84	3.93 \pm 1.19				78.58 \pm 1.39	8.16 \pm 2.13		
bSAM	97.54 \pm 0.01	4.31 \pm 0.01				79.12 \pm 0.01	6.11 \pm 0.03		
SGLD	97.84 \pm 0.26	8.79 \pm 1.77				78.18 \pm 0.72	9.74 \pm 1.55		
Entropy-SGLD	95.89 \pm 2.64	16.35 \pm 8.76				77.50 \pm 2.50	6.85 \pm 3.57		
EMCMC	98.65 \pm 0.52	2.93 \pm 0.65				79.96 \pm 0.52	4.06 \pm 0.18		

6.5 UNCERTAINTY AND OOD DETECTION

To illustrate how predictive uncertainty estimation benefits from flat basins, we evaluate EMCMC on out-of-distribution (OOD) detection. We train each model on CIFAR and quantify uncertainty using the entropy of predictive distributions (Malinin & Gales, 2018). Then we use the uncertainty to detect SVHN samples in a joint testing set combined by CIFAR and SVHN (Netzer et al., 2011). We evaluate each algorithm with Area under ROC Curve (AUC) (McClish, 1989) and Expected Calibration Error (ECE) (Naeini et al., 2015). All other settings remain the same as the classification experiments. Table 2 shows the evaluation results, where EMCMC outperforms all baselines, especially on the ECE metric. This indicates that predictive uncertainty estimation is more accurate if the samples are from flat basins of the posterior.

7 CONCLUSION AND DISCUSSION

We propose a practical MCMC algorithm to sample from flat basins of DNN posterior distributions. Specifically, we introduce a guiding variable based on the local entropy to steer the MCMC sampler toward flat basins. The joint distribution of this variable and the model parameter enjoys a simple form which enables efficient sampling. We prove the fast convergence rate of our method compared with two existing flatness-aware methods. Comprehensive experiments demonstrate the superiority of our method, verifying that it can sample from flat basins and achieve outstanding performance on diverse tasks. Our method is mathematically simple and computationally efficient, allowing for adoption as a drop-in replacement for standard sampling methods such as SGLD.

The results hold promise for both Bayesian methods and deep learning generalization. On the one hand, we demonstrate that explicitly considering flatness in Bayesian deep learning can significantly improve generalization, robustness, and uncertainty estimation, especially under practical computational constraints. On the other hand, we highlight the value of marginalizing over flat basins in the energy landscape, as a means to attain further performance improvements compared to single point optimization methods.

REFERENCES

- Ahmad Ajalloeian and Sebastian U. Stich. On the convergence of sgd with biased gradients. *Journal of Machine Learning Research*, 2020. URL <https://api.semanticscholar.org/CorpusID:234358812>.
- Christophe Andrieu, Nando De Freitas, Arnaud Doucet, and Michael I Jordan. An introduction to mcmc for machine learning. *Machine learning*, 50:5–43, 2003.
- Dara Bahri, Hossein Mobahi, and Yi Tay. Sharpness-aware minimization improves language model generalization. In *Proceedings of the 60th Annual Meeting of the Association for Computational Linguistics (Volume 1: Long Papers)*, pp. 7360–7371, 2022.
- Carlo Baldassi, Christian Borgs, Jennifer T Chayes, Alessandro Ingrosso, Carlo Lucibello, Luca Saglietti, and Riccardo Zecchina. Unreasonable effectiveness of learning neural networks: From accessible states and robust ensembles to basic algorithmic schemes. *Proceedings of the National Academy of Sciences*, 113(48):E7655–E7662, 2016.
- Christopher M Bishop. *Pattern recognition and machine learning*, volume 4. Springer, 2006.
- Devansh Bisla, Jing Wang, and Anna Choromanska. Low-pass filtering sgd for recovering flat optima in the deep learning optimization landscape. In *International Conference on Artificial Intelligence and Statistics*, pp. 8299–8339. PMLR, 2022.
- Pratik Chaudhari, Anna Choromanska, Stefano Soatto, Yann LeCun, Carlo Baldassi, Christian Borgs, Jennifer Chayes, Levent Sagun, and Riccardo Zecchina. Entropy-sgd: Biasing gradient descent into wide valleys. *Journal of Statistical Mechanics: Theory and Experiment*, 2019(12):124018, 2019.
- Tianqi Chen, Emily Fox, and Carlos Guestrin. Stochastic gradient hamiltonian monte carlo. In *International conference on machine learning*, pp. 1683–1691. PMLR, 2014.
- Adam D Cobb and Brian Jalaian. Scaling hamiltonian monte carlo inference for bayesian neural networks with symmetric splitting. In *Uncertainty in Artificial Intelligence*, pp. 675–685. PMLR, 2021.
- Arnak S Dalalyan and Avetik Karagulyan. User-friendly guarantees for the langevin monte carlo with inaccurate gradient. *Stochastic Processes and their Applications*, 129(12):5278–5311, 2019.
- Jia Deng, Wei Dong, Richard Socher, Li-Jia Li, Kai Li, and Li Fei-Fei. Imagenet: A large-scale hierarchical image database. In *2009 IEEE conference on computer vision and pattern recognition*, pp. 248–255. Ieee, 2009.
- Laurent Dinh, Razvan Pascanu, Samy Bengio, and Yoshua Bengio. Sharp minima can generalize for deep nets. In *International Conference on Machine Learning*, pp. 1019–1028. PMLR, 2017.
- Gintare Karolina Dziugaite and Daniel Roy. Entropy-sgd optimizes the prior of a pac-bayes bound: Generalization properties of entropy-sgd and data-dependent priors. In *International Conference on Machine Learning*, pp. 1377–1386. PMLR, 2018.
- Pierre Foret, Ariel Kleiner, Hossein Mobahi, and Behnam Neyshabur. Sharpness-aware minimization for efficiently improving generalization. In *International Conference on Learning Representations*, 2020.
- Alan E Gelfand. Gibbs sampling. *Journal of the American statistical Association*, 95(452):1300–1304, 2000.
- Kaiming He, Xiangyu Zhang, Shaoqing Ren, and Jian Sun. Deep residual learning for image recognition. In *Proceedings of the IEEE conference on computer vision and pattern recognition*, pp. 770–778, 2016.
- Dan Hendrycks and Thomas Dietterich. Benchmarking neural network robustness to common corruptions and perturbations. In *International Conference on Learning Representations*, 2018.

-
- Dan Hendrycks and Thomas Dietterich. Benchmarking neural network robustness to common corruptions and perturbations. *Proceedings of the International Conference on Learning Representations*, 2019a.
- Dan Hendrycks and Thomas Dietterich. Benchmarking neural network robustness to common corruptions and perturbations. In *International Conference on Learning Representations*, 2019b.
- Sepp Hochreiter and Jürgen Schmidhuber. Simplifying neural nets by discovering flat minima. *Advances in neural information processing systems*, 7, 1994.
- Sepp Hochreiter and Jürgen Schmidhuber. Flat minima. *Neural computation*, 9(1):1–42, 1997.
- W Ronny Huang, Zeyad Ali Sami Emam, Micah Goldblum, Liam H Fowl, JK Terry, Furong Huang, and Tom Goldstein. Understanding generalization through visualizations. In *"I Can't Believe It's Not Better!" NeurIPS workshop*, 2020.
- P Izmailov, AG Wilson, D Podoprikin, D Vetrov, and T Garipov. Averaging weights leads to wider optima and better generalization. In *34th Conference on Uncertainty in Artificial Intelligence 2018, UAI 2018*, pp. 876–885, 2018.
- Pavel Izmailov, Sharad Vikram, Matthew D Hoffman, and Andrew Gordon Gordon Wilson. What are bayesian neural network posteriors really like? In *International conference on machine learning*, pp. 4629–4640. PMLR, 2021.
- Yiding Jiang, Behnam Neyshabur, Hossein Mobahi, Dilip Krishnan, and Samy Bengio. Fantastic generalization measures and where to find them. In *International Conference on Learning Representations*, 2019a.
- Yiding Jiang, Behnam Neyshabur, Hossein Mobahi, Dilip Krishnan, and Samy Bengio. Fantastic generalization measures and where to find them. In *International Conference on Learning Representations*, 2019b.
- Nitish Shirish Keskar, Jorge Nocedal, Ping Tak Peter Tang, Dheevatsa Mudigere, and Mikhail Smelyanskiy. On large-batch training for deep learning: Generalization gap and sharp minima. In *5th International Conference on Learning Representations, ICLR 2017*, 2017.
- A Krizhevsky. Learning multiple layers of features from tiny images. *Master's thesis, University of Tront*, 2009.
- Yann LeCun. The mnist database of handwritten digits. <http://yann.lecun.com/exdb/mnist/>, 1998.
- Mu Li, Tong Zhang, Yuqiang Chen, and Alexander J Smola. Efficient mini-batch training for stochastic optimization. In *Proceedings of the 20th ACM SIGKDD international conference on Knowledge discovery and data mining*, pp. 661–670, 2014.
- Yi-An Ma, Tianqi Chen, and Emily Fox. A complete recipe for stochastic gradient mcmc. *Advances in neural information processing systems*, 28, 2015.
- Dougal Maclaurin and Ryan P Adams. Firefly monte carlo: exact mcmc with subsets of data. In *Proceedings of the 24th International Conference on Artificial Intelligence*, pp. 4289–4295, 2015.
- Andrey Malinin and Mark Gales. Predictive uncertainty estimation via prior networks. *Advances in neural information processing systems*, 31, 2018.
- Donna Katzman McClish. Analyzing a portion of the roc curve. *Medical decision making*, 9(3): 190–195, 1989.
- Hossein Mobahi. Training recurrent neural networks by diffusion. *arXiv preprint arXiv:1601.04114*, 2016.
- Thomas Möllenhoff and Mohammad Emtiyaz Khan. Sam as an optimal relaxation of bayes. In *The Eleventh International Conference on Learning Representations*, 2022.

-
- Mahdi Pakdaman Naeini, Gregory Cooper, and Milos Hauskrecht. Obtaining well calibrated probabilities using bayesian binning. In *Proceedings of the AAAI conference on artificial intelligence*, volume 29, 2015.
- Radford M Neal. *Bayesian learning for neural networks*, volume 118. Springer Science & Business Media, 2012.
- Yuval Netzer, Tao Wang, Adam Coates, Alessandro Bissacco, Bo Wu, and Andrew Y Ng. Reading digits in natural images with unsupervised feature learning. *NIPS Workshop on Deep Learning and Unsupervised Feature Learning*, 2011.
- Behnam Neyshabur, Srinadh Bhojanapalli, David McAllester, and Nati Srebro. Exploring generalization in deep learning. *Advances in neural information processing systems*, 30, 2017.
- Saurabh Singh and Shankar Krishnan. Filter response normalization layer: Eliminating batch dependence in the training of deep neural networks. In *Proceedings of the IEEE/CVF conference on computer vision and pattern recognition*, pp. 11237–11246, 2020.
- Larry Wasserman. *All of statistics: a concise course in statistical inference*, volume 26. Springer, 2004.
- Max Welling and Yee W Teh. Bayesian learning via stochastic gradient langevin dynamics. In *Proceedings of the 28th international conference on machine learning (ICML-11)*, pp. 681–688, 2011.
- Andrew Gordon Wilson. The case for bayesian deep learning. *arXiv preprint arXiv:2001.10995*, 2020.
- Ruqi Zhang, A Feder Cooper, and Christopher M De Sa. Asymptotically optimal exact minibatch metropolis-hastings. *Advances in Neural Information Processing Systems*, 33:19500–19510, 2020a.
- Ruqi Zhang, Chunyuan Li, Jianyi Zhang, Changyou Chen, and Andrew Gordon Wilson. Cyclical stochastic gradient mcmc for bayesian deep learning. In *International Conference on Learning Representations*, 2020b.

A ALGORITHM DETAILS

We list some details of the proposed Entropy-MCMC in this section, to help understanding our code and reproduction. As discussed in section 4.2, the updating rule of Entropy-MCMC can be written as:

$$\tilde{\boldsymbol{\theta}} \leftarrow \tilde{\boldsymbol{\theta}} - \alpha \nabla_{\tilde{\boldsymbol{\theta}}} U(\tilde{\boldsymbol{\theta}}) + \sqrt{2\alpha} \cdot \boldsymbol{\epsilon}, \quad (11)$$

which is a full-batch version. We will show how to apply modern deep learning techniques like mini-batching and temperature to the updating policy in the following section.

A.1 MINI-BATCHING

We adopt the standard mini-batching technique in our method, which samples a subset of data points per iteration (Li et al., 2014). We assume the entire dataset to be $\mathcal{D} = \{(\mathbf{x}_i, y_i)\}_{i=1}^N$. Then a batch sampled from \mathcal{D} is $\Xi = \{(\mathbf{x}_i, y_i)\}_{i=1}^M \subset \mathcal{D}$ with $M \ll N$. For the entire dataset, the loss function is computed by:

$$f(\boldsymbol{\theta}) \propto - \sum_{i=1}^N \log p(y_i | \mathbf{x}_i, \boldsymbol{\theta}) - \log p(\boldsymbol{\theta}), \quad (12)$$

and in order to balance the updating stride per iteration, the loss function for a mini-batch is:

$$f_{\Xi}(\boldsymbol{\theta}) \propto - \frac{N}{M} \sum_{i=1}^M \log p(y_i | \mathbf{x}_i, \boldsymbol{\theta}) - \log p(\boldsymbol{\theta}). \quad (13)$$

Therefore, if we average the mini-batch loss over all data points, we can obtain the following form:

$$\bar{f}_{\Xi}(\boldsymbol{\theta}) \propto - \frac{1}{M} \sum_{i=1}^M \log p(y_i | \mathbf{x}_i, \boldsymbol{\theta}) - \frac{1}{N} \log p(\boldsymbol{\theta}). \quad (14)$$

If we regard the averaging process as a modification on the stepsize α (i.e., $\bar{\alpha} = \alpha/N$), we will have the following form for the updating policy:

$$\begin{aligned} \Delta \tilde{\boldsymbol{\theta}} &= -\bar{\alpha} \cdot \nabla_{\tilde{\boldsymbol{\theta}}} \tilde{U}(\tilde{\boldsymbol{\theta}}) + \sqrt{2\bar{\alpha}} \cdot \boldsymbol{\epsilon} \\ &= -\bar{\alpha} \cdot \nabla_{\tilde{\boldsymbol{\theta}}} \left[f_{\Xi}(\boldsymbol{\theta}) + \frac{1}{2\eta} \|\boldsymbol{\theta} - \boldsymbol{\theta}_a\|^2 - \sqrt{\frac{2}{\bar{\alpha}}} \boldsymbol{\epsilon} \odot \tilde{\boldsymbol{\theta}} \right] \\ &= -\alpha \cdot \nabla_{\tilde{\boldsymbol{\theta}}} \left[\bar{f}_{\Xi}(\boldsymbol{\theta}) + \frac{1}{2\eta N} \|\boldsymbol{\theta} - \boldsymbol{\theta}_a\|^2 - \sqrt{\frac{2}{\alpha N}} \boldsymbol{\epsilon} \odot \tilde{\boldsymbol{\theta}} \right]. \end{aligned} \quad (15)$$

Therefore, the updating rule in Eq.11 can be equivalently written as:

$$\tilde{\boldsymbol{\theta}} \leftarrow \tilde{\boldsymbol{\theta}} - \Delta \tilde{\boldsymbol{\theta}}. \quad (16)$$

A.2 DATA AUGMENTATION AND TEMPERATURE

We apply data augmentation, which is commonly used in deep neural networks, and compare all methods with data augmentation in the main text. Here, we additionally compare the classification results without data augmentation in Table 3 to demonstrate the effectiveness of EMCMC in this case.

Table 3: Comparison of data augmentation of 3 baselines on CIFAR10. EMCMC outperforms previous methods with and without data augmentation.

Augmentation	SGD	SGLD	EMCMC
×	89.60	89.24	89.87
✓	95.59	95.64	95.79

Besides, in the updating policy, a noise term is introduced to add randomness to the sampling process. However, in mini-batch training, the effect of noise will be amplified so that the stationary

distribution of might be far away from the true posterior distribution (Zhang et al., 2020b). Therefore, we also introduce a system temperature T to address this problem.

Formally, the posterior distribution is tempered to be $p(\boldsymbol{\theta}|\mathcal{D}) \propto \exp(-U(\boldsymbol{\theta})/T)$, with an averagely sharpened energy landscape. Similarly, we can regard the temperature effect as a new stepsize $\alpha_T = \alpha/T$, and the updating policy would be:

$$\begin{aligned} \Delta \tilde{\boldsymbol{\theta}} &= -\alpha \cdot \nabla_{\tilde{\boldsymbol{\theta}}} \left[\left(\bar{f}_{\Xi}(\boldsymbol{\theta}) + \frac{1}{2\eta N} \|\boldsymbol{\theta} - \boldsymbol{\theta}_a\|^2 \right) / T - \sqrt{\frac{2}{\alpha N}} \boldsymbol{\epsilon} \odot \tilde{\boldsymbol{\theta}} \right] \\ &= -\alpha_T \cdot \nabla_{\tilde{\boldsymbol{\theta}}} \left[\bar{f}_{\Xi}(\boldsymbol{\theta}) + \frac{1}{2\eta N} \|\boldsymbol{\theta} - \boldsymbol{\theta}_a\|^2 - \sqrt{\frac{2T}{\alpha_T N}} \boldsymbol{\epsilon} \odot \tilde{\boldsymbol{\theta}} \right]. \end{aligned} \quad (17)$$

In order to empirically determine the best temperature, we compare different temperature level in table 4, and find that $T = 10^{-4}$ is appropriate for classification task.

Table 4: Comparison of temperature effect on CIFAR10 with data augmentation. $T = 10^{-4}$ is best temperature level.

T	1	1e-1	1e-2	1e-3	1e-4	1e-5
Testing ACC (%) \uparrow	95.30	95.42	95.41	95.48	95.50	95.47

A.3 GIBBS-LIKE UPDATING PROCEDURE

Instead of jointly updating, we can also choose to alternatively update $\boldsymbol{\theta}$ and $\boldsymbol{\theta}_a$. The conditional distribution for the model $\boldsymbol{\theta}$ is:

$$p(\boldsymbol{\theta}|\boldsymbol{\theta}_a, \mathcal{D}) = \frac{p(\boldsymbol{\theta}, \boldsymbol{\theta}_a|\mathcal{D})}{p(\boldsymbol{\theta}_a|\mathcal{D})} \propto \frac{1}{Z_{\boldsymbol{\theta}_a}} \exp \left\{ -f(\boldsymbol{\theta}) - \frac{1}{2\eta} \|\boldsymbol{\theta} - \boldsymbol{\theta}_a\|^2 \right\}, \quad (18)$$

where $Z_{\boldsymbol{\theta}_a} = \exp \mathcal{F}(\boldsymbol{\theta}_a; \eta)$ is a constant. While for the guiding variable $\boldsymbol{\theta}_a$, its conditional distribution is:

$$p(\boldsymbol{\theta}_a|\boldsymbol{\theta}, \mathcal{D}) = \frac{p(\boldsymbol{\theta}, \boldsymbol{\theta}_a|\mathcal{D})}{p(\boldsymbol{\theta}|\mathcal{D})} \propto \frac{1}{Z_{\boldsymbol{\theta}}} \exp \left\{ -\frac{1}{2\eta} \|\boldsymbol{\theta} - \boldsymbol{\theta}_a\|^2 \right\}, \quad (19)$$

where $Z_{\boldsymbol{\theta}} = \exp(-f(\boldsymbol{\theta}))$ is a constant. Therefore, with Gaussian noise, $\boldsymbol{\theta}_a$ is equivalently sampled from $\mathcal{N}(\boldsymbol{\theta}, \eta \mathbf{I})$, and the variance η controls the expected distance between $\boldsymbol{\theta}$ and $\boldsymbol{\theta}_a$. To obtain samples from the joint distribution, we can sample from $p(\boldsymbol{\theta}|\boldsymbol{\theta}_a, \mathcal{D})$ and $p(\boldsymbol{\theta}_a|\boldsymbol{\theta}, \mathcal{D})$ alternatively. The advantage of doing Gibbs-like updating is that sampling $\boldsymbol{\theta}_a$ can be done exactly. Empirically, we observe that joint updating yields superior performance compared to Gibbs-like updating due to the efficiency of updating both $\boldsymbol{\theta}$ and $\boldsymbol{\theta}_a$ at the same time.

B PROOF OF THEOREMS

B.1 LEMMA 1

Proof. Assume $\tilde{\boldsymbol{\theta}} = [\boldsymbol{\theta}^T, \boldsymbol{\theta}_a^T]^T$ is sampled from the joint posterior distribution:

$$p(\tilde{\boldsymbol{\theta}}|\mathcal{D}) = p(\boldsymbol{\theta}, \boldsymbol{\theta}_a|\mathcal{D}) \propto \exp \left\{ -f(\boldsymbol{\theta}) - \frac{1}{2\eta} \|\boldsymbol{\theta} - \boldsymbol{\theta}_a\|^2 \right\}. \quad (20)$$

Then the marginal distribution respectively for $\boldsymbol{\theta}$ and $\boldsymbol{\theta}_a$ would be:

$$\begin{aligned} p(\boldsymbol{\theta}|\mathcal{D}) &= \int_{\boldsymbol{\theta}_a} p(\boldsymbol{\theta}, \boldsymbol{\theta}_a|\mathcal{D}) d\boldsymbol{\theta}_a \\ &= \int_{\boldsymbol{\theta}_a} \exp \left\{ -f(\boldsymbol{\theta}) - \frac{1}{2\eta} \|\boldsymbol{\theta} - \boldsymbol{\theta}_a\|^2 \right\} d\boldsymbol{\theta}_a \\ &= \exp(-f(\boldsymbol{\theta})) \int_{\boldsymbol{\theta}_a} \exp \left\{ -\frac{1}{2\eta} \|\boldsymbol{\theta} - \boldsymbol{\theta}_a\|^2 \right\} d\boldsymbol{\theta}_a \\ &= \exp(-f(\boldsymbol{\theta})), \end{aligned} \quad (21)$$

and similarly we have

$$\begin{aligned}
p(\boldsymbol{\theta}_a|\mathcal{D}) &= \int_{\Theta} p(\boldsymbol{\theta}, \boldsymbol{\theta}_a|\mathcal{D})d\boldsymbol{\theta} \\
&= \int_{\Theta} \exp\left\{-f(\boldsymbol{\theta}) - \frac{1}{2\eta}\|\boldsymbol{\theta} - \boldsymbol{\theta}_a\|^2\right\}d\boldsymbol{\theta} \\
&= \exp \mathcal{F}(\boldsymbol{\theta}_a; \eta).
\end{aligned} \tag{22}$$

□

B.2 LEMMA 2

Proof. Note that we have

$$-\nabla^2 \log \pi_{\text{joint}} = \begin{bmatrix} \nabla^2 f(\theta') + \frac{1}{\eta}I & -\frac{1}{\eta}I \\ -\frac{1}{\eta}I & \frac{1}{\eta}I \end{bmatrix},$$

and after a row reduction, we get

$$\begin{bmatrix} \nabla^2 f(\theta') & 0 \\ -\frac{1}{\eta}I & \frac{1}{\eta}I \end{bmatrix}.$$

The eigenvalues for this matrix are the eigenvalues of $\nabla^2 f(\theta')$ and $1/\eta$. By the assumption $m \leq 1/\eta \leq M$, we have

$$mI \preceq \begin{bmatrix} \nabla^2 f(\theta') & 0 \\ -\frac{1}{\eta}I & \frac{1}{\eta}I \end{bmatrix} \preceq MI,$$

which means $-\nabla^2 \log \pi_{\text{joint}}$ is also a M -smooth and m -strongly convex function.

In most scenarios, m often takes on very small values and M tends to be very large. Therefore, the assumption $m \leq 1/\eta \leq M$ is mild. □

B.3 PROOF OF THEOREM 1

Proof. The proof relies on Theorem 4 from Dalalyan & Karagulyan (2019). Lemma 2 has already provided us with the smoothness and strong convexity parameters for π_{joint} . We will now address the bias and variance of stochastic gradient estimation. The stochastic gradient is given by $[\nabla \tilde{f}(\theta') + \frac{1}{\eta}(\theta' - \theta), -\frac{1}{\eta}(\theta' - \theta)]^T$. As $\nabla \tilde{f}(\theta')$ is unbiased and has a variance of σ^2 , the stochastic gradient in our method is also unbiased and has variance σ^2 . Combining the above results, we are ready to apply Theorem 4 (Dalalyan & Karagulyan, 2019) and obtain

$$W_2(\mu_K, \pi_{\text{joint}}) \leq (1 - \alpha m)^K W_2(\mu_0, \pi) + 1.65(M/m)(2\alpha d)^{1/2} + \frac{\sigma^2(2\alpha d)^{1/2}}{1.65M + \sigma\sqrt{m}}.$$

□

B.4 THEOREM 3

Proof. Let $\pi'(\theta') \propto \exp(-f(\theta') - \frac{1}{2\eta}\|\theta' - \theta\|_2^2)$. It is easy to see that $m + 1/\eta \preceq \nabla^2(-\log \pi') \preceq M + 1/\eta$. Based on Theorem 4 in Dalalyan & Karagulyan (2019), the 2-Wasserstein distance for the inner Markov chain is

$$\begin{aligned}
W_2(\zeta_L, \pi') &\leq (1 - \alpha m)^L W_2(\zeta_0, \pi') + 1.65 \left(\frac{M + 1/\eta}{m + 1/\eta}\right) (\alpha d)^{1/2} + \frac{\sigma^2(\alpha d)^{1/2}}{1.65(M + 1/\eta) + \sigma\sqrt{m + 1/\eta}} \\
&\leq (1 - \alpha m)^L \kappa + 1.65 \left(\frac{M + 1/\eta}{m + 1/\eta}\right) (\alpha d)^{1/2} + \frac{\sigma^2(\alpha d)^{1/2}}{1.65(M + 1/\eta) + \sigma\sqrt{m + 1/\eta}} \\
&:= A^2.
\end{aligned}$$

Now we consider the convergence of the outer Markov chain. We denote $\pi_{\text{flat}}(\theta) \propto \exp \mathcal{F}(\theta; \eta)$. From Chaudhari et al. (2019), we know that

$$\inf_{\theta} \left\| \frac{1}{I + \eta \nabla^2 f(\theta)} \right\| mI \preceq -\nabla^2 \log \pi_{\text{flat}} \preceq \sup_{\theta} \left\| \frac{1}{I + \eta \nabla^2 f(\theta)} \right\| MI.$$

Since $mI \preceq \nabla^2 f(\theta) \preceq MI$, it follows

$$\inf_{\theta} \left\| \frac{1}{I + \eta \nabla^2 f(\theta)} \right\| \geq \frac{1}{1 + \eta M}, \quad \sup_{\theta} \left\| \frac{1}{I + \eta \nabla^2 f(\theta)} \right\| \leq \frac{1}{1 + \eta m}.$$

Therefore,

$$\frac{m}{1 + \eta M} I \preceq -\nabla^2 \log \pi_{\text{flat}} \preceq \frac{M}{1 + \eta m} I.$$

The update rule of the outer SGLD is

$$\theta = \theta - \alpha/\eta(\theta - \mathbf{E}_{\zeta_L}[\theta']) + \sqrt{2\alpha}\xi.$$

The gradient estimation can be written as $\theta - \mathbf{E}_{\pi'}[\theta'] + (\mathbf{E}_{\pi'}[\theta'] - \mathbf{E}_{\zeta_L}[\theta'])$ which can be regarded as the true gradient $\theta - \mathbf{E}_{\pi'}[\theta']$ plus some noise $(\mathbf{E}_{\pi'}[\theta'] - \mathbf{E}_{\zeta_L}[\theta'])$. The bias of the noise can be bounded as follows

$$\begin{aligned} \|\mathbf{E}_{\pi'}[\theta'] - \mathbf{E}_{\zeta_L}[\theta']\|_2^2 &= \left\| \int [\theta'_{\pi'} - \theta'_{\zeta_L}] dJ(\theta'_{\pi'}, \theta'_{\zeta_L}) \right\|_2^2 \\ &\leq \int \|\theta'_{\pi'} - \theta'_{\zeta_L}\|_2^2 dJ(\theta'_{\pi'}, \theta'_{\zeta_L}). \end{aligned}$$

Since the inequality holds for any J , we can take the infimum over all possible distributions to conclude

$$\|\mathbf{E}_{\pi'}[\theta'] - \mathbf{E}_{\zeta_L}[\theta']\|_2^2 \leq W_2(\zeta_L, \pi').$$

Furthermore, we note that the variance of the noise is zero. Therefore, by applying Theorem 4 in Dalalyan & Karagulyan (2019) we get

$$W_2(\nu_K, \pi_{\text{flat}}) \leq (1 - \alpha m)^K W_2(\nu_0, \pi_{\text{flat}}) + 1.65 \left(\frac{1 + \eta M}{1 + \eta m} \right) (M/m)(\alpha d)^{1/2} + \frac{A(1 + \eta M)}{m}. \quad \square$$

B.5 THEOREM 2

Proof. Compared to Entropy-SGLD, the only difference of Entropy-SGD is to do SGD update instead of SGLD update in the outer loop. Therefore, the analysis for the inner Markov chain remains the same as in Theorem 3. To analyze the error of SGD in the outer loop, we follow the results in Ajalloeian & Stich (2020). Since the strongly convex parameter for f_{flat} is $\frac{m}{1 + \eta M}$, by Section 4.2 and Assumption 4 in Ajalloeian & Stich (2020), we know that

$$\begin{aligned} \frac{1}{2} \|\nabla f_{\text{flat}}(\theta_t)\|^2 &\leq \frac{E_t - E_{t+1}}{\alpha} + \frac{1}{2}A \\ \Rightarrow \frac{m}{1 + \eta M} E_t &\leq \frac{E_t - E_{t+1}}{\alpha} + \frac{1}{2}A \\ \Rightarrow E_{t+1} &\leq \left(1 - \frac{\alpha m}{1 + \eta M}\right) E_t + \frac{1}{2}\alpha A. \end{aligned}$$

By unrolling the recursion, we obtain

$$E_K \leq \left(1 - \frac{\alpha m}{1 + \eta M}\right)^K E_0 + \frac{A(1 + \eta M)}{2m}. \quad \square$$

C ABLATION STUDIES

We empirically discuss several important hyper-parameters and algorithm settings in this section, which justifies our choice of their values.

C.1 VARIANCE TERM

We compare different choices of the variance term η to determine the best value for each dataset. The experimental results are shown in Fig. 6. Generally, the best η for CIFAR100 is about 10^{-2} and for CIFAR10 is about 10^{-3} , which implies that the energy landscapes of CIFAR10 and CIFAR100 may be different.

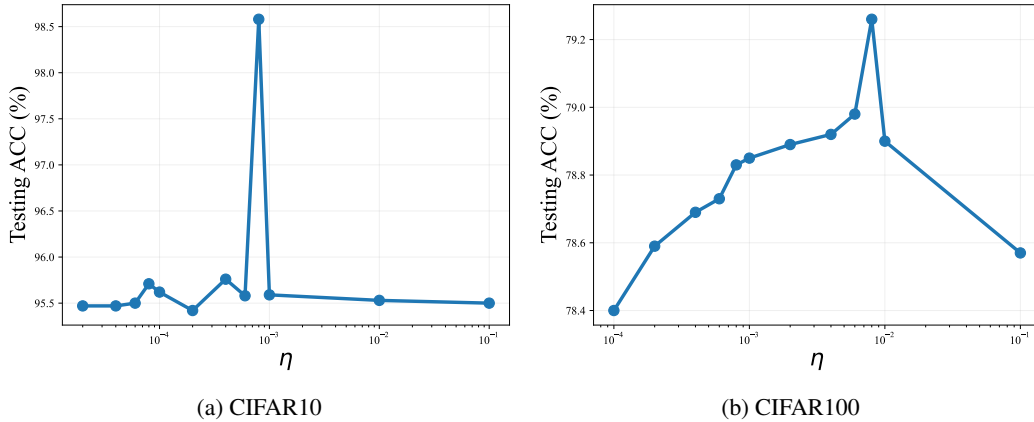


Figure 6: Comparison of different variance level for Entropy algorithm. $\eta \approx 10^{-3}$ is the best on CIFAR10, and $\eta \approx 10^{-2}$ is the best on CIFAR100.

C.2 STEP SIZE SCHEDULES

We compare different types of stepsize schedules in Table 6. Specifically, we assume the initial and final stepsize to be α_0 and α_1 respectively. T is the total number of epochs and t is the current epoch. The detailed descriptions of stepsize schedules are listed in Table 5. The cyclical stepsize is the best among all stepsize schedules.

Table 5: Formulas or descriptions of different stepsize schedules.

Name	Formula/Description
constant	$\alpha(t) = \alpha_0$
linear	$\alpha(t) = \frac{T-t}{T}(\alpha_0 - \alpha_1) + \alpha_1$
exponential	$\alpha(t) = \alpha_0 \cdot (\alpha_1/\alpha_0)^{t/T}$
step	Remain the same stepsize within one ‘‘step’’, and decay between ‘‘steps’’.
cyclical	Follow Eq. 1 in Zhang et al. (2020b).

Table 6: Comparison of stepsize schedules on CIFAR100. The cyclical stepsize is the best for Entropy-MCMC.

Learning Rate Schedule	constant	linear	exponential	step	cyclical
Testing ACC (%) \uparrow	88.04	87.89	87.75	89.59	89.93

C.3 COLLECTING SAMPLES

Due to the introduction of the auxiliary guiding variable θ_a , the composition of sample set \mathcal{S} has multiple choices: only collect samples of θ , only collect samples of θ_a , collect both samples. We conduct the comparison of all choices and the results are reported in Table 7. It shows that using samples from both θ and θ_a gives the best generalization accuracy.

Table 7: Ablation study on the composition of sample set \mathcal{S} on CIFAR10. With samples from both θ and θ_a , the Bayesian marginalization can achieve the best accuracy.

θ	θ_a	ACC (%) \uparrow
✓		95.58
	✓	95.64
✓	✓	95.65

C.4 NORMALIZATION LAYERS

During testing, the usage of bath normalization layers (BN) in the model architecture induces a problem regarding the mini-batch statistics. The mean and variance of a batch need calculated through at least one forward pass, which is not applicable for the guiding variable θ_a since it is updated by the distance regularization during training. We try different solutions for this problem, including one additional forward pass and the Filter Response Normalization (Singh & Krishnan, 2020). The comparison is listed in Table 8, where simply adding one additional forward pass during testing can achieve promising accuracy with negligible computational overhead.

Table 8: Comparison of different normalization layers on CIFAR10. Simply adding one additional forward pass during testing with standard batch normalization is the best solution.

Normalization Layer	ACC (%) \uparrow	Time (h)
BN	95.40	1.8
BN (one additional forward)	95.47	1.9
FRN (Singh & Krishnan, 2020)	93.92	2.5

C.5 SGD BURN-IN

We also try SGD burn-in in our ablation studies, by adding the random noise term only to the last few epochs to ensure the fast convergence. We evaluate different settings of SGD burn-in epochs in Table 9. We find that adding 40 burn-in epochs per 50 epochs is the best choice.

Table 9: Comparison of different SGD burn-in epochs on CIFAR10. In a 50-epoch round, using SGD burn-in in the first 40 epochs is the best choice.

SGD Burn-in Epoch	0	10	20	30	40	47
Test ACC (%) \uparrow	95.61	95.62	95.57	95.67	95.72	95.41

D ADDITIONAL EXPERIMENTAL RESULTS

We list the additional experimental results in this section, to demonstrate the superiority of our method and show some interesting findings.

D.1 ADDITIONAL SYNTHETIC EXAMPLES

To demonstrate that EMCMC can bias toward the flat mode under random initialization, we conduct additional synthetic experiments under two different initialization settings. Specifically, we set the initial point to be $(-0.4, -0.4)$ to prefer the sharp mode (Fig. 7) and $(0.0, 0.0)$ to prefer the flat mode (Fig. 8). It is clear that EMCMC can find the flat mode under all initialization settings, while SGD and SGLD are heavily affected by the choices of initialization.

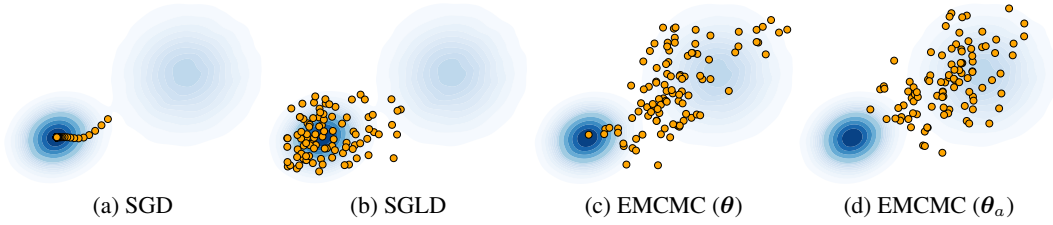


Figure 7: Synthetic Experiments with sharp-mode-biased initialization.

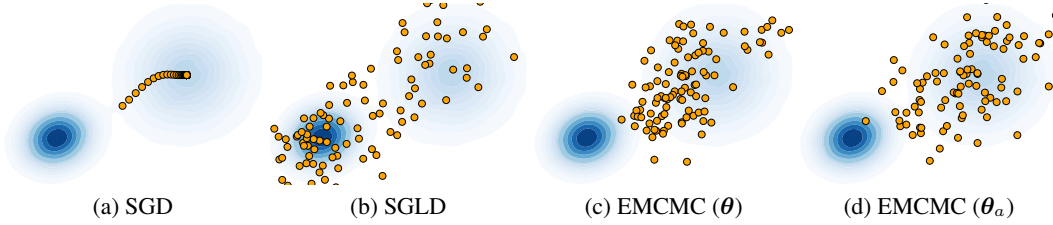


Figure 8: Synthetic Experiments with flat-mode-biased initialization.

D.2 PARAMETER SPACE INTERPOLATION

As the supplement for Fig. 5, we show additional interpolation results to demonstrate some interesting findings about the model θ and the auxiliary guiding variable θ_a . The additional interpolation can be separated into the following types:

D.2.1 TOWARD RANDOM DIRECTIONS.

We show the interpolation results toward averaged random directions (10 random directions) in Fig. 9. For the training loss, the auxiliary guiding variable θ is located at a flatter local region with relatively larger loss values. While for the testing error, the guiding variable θ_a consistently has lower generation errors, which illustrates that the flat modes are more preferable in terms of generalization.

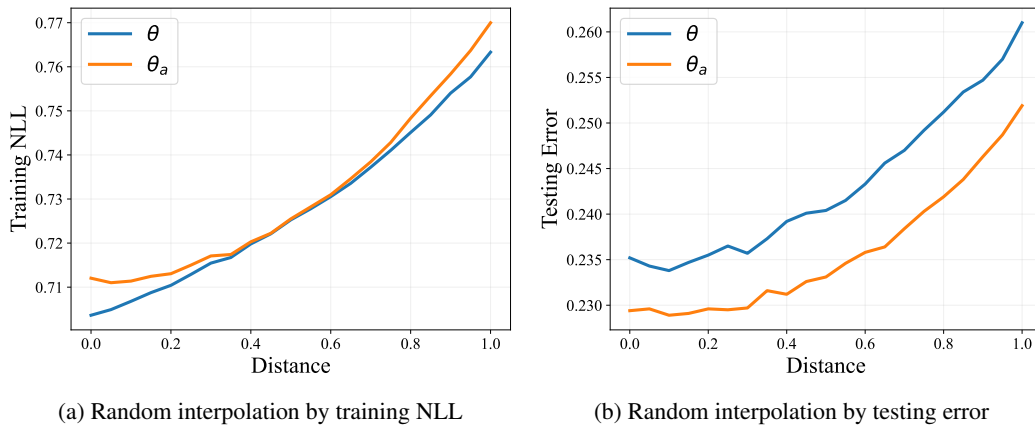


Figure 9: Interpolation toward averaged random directions on CIFAR100, comparing the model θ and the guiding variable θ_a .

D.2.2 BETWEEN MODEL PARAMETER AND GUIDING VARIABLE.

The line between the model parameter θ and the guiding variable θ_a is a special direction in the parameter space. The NLL and testing error are both much lower than random directions, which is shown in Fig. 10. Besides, this special direction is biased toward the local region of θ_a , with averagely lower testing errors. This finding justifies the setting of adding θ_a to the sample set \mathcal{S} , since the generalization performance of θ_a is better.

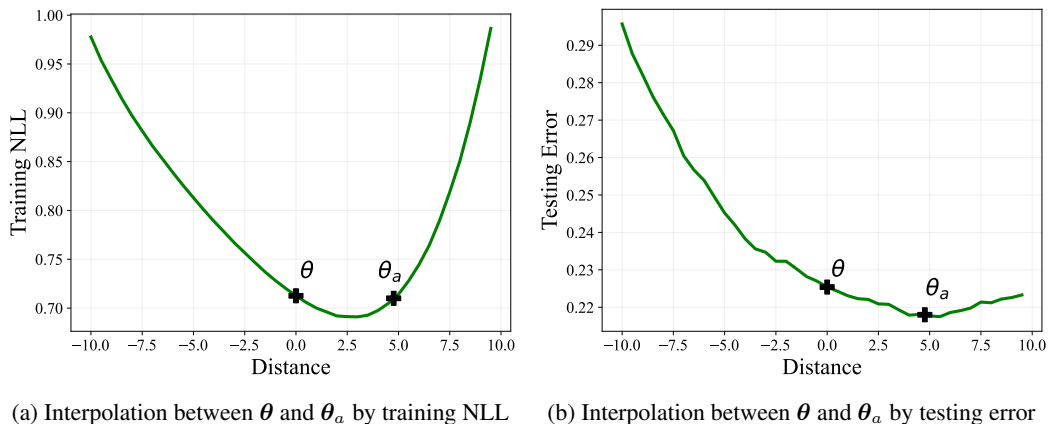


Figure 10: Interpolation between the model θ and the guiding variable θ_a in terms of training NLL and testing error on CIFAR100.

D.3 CLASSIFICATION ON CORRUPTED CIFAR

We list the detailed classification results on corrupted CIFAR (Hendrycks & Dietterich, 2018) in Fig. 11, where each corruption type is evaluated at a corresponding subfigure. For the majority of corruption types, our method outperforms other baselines under all severity levels, and is superior especially under sever corruptions.

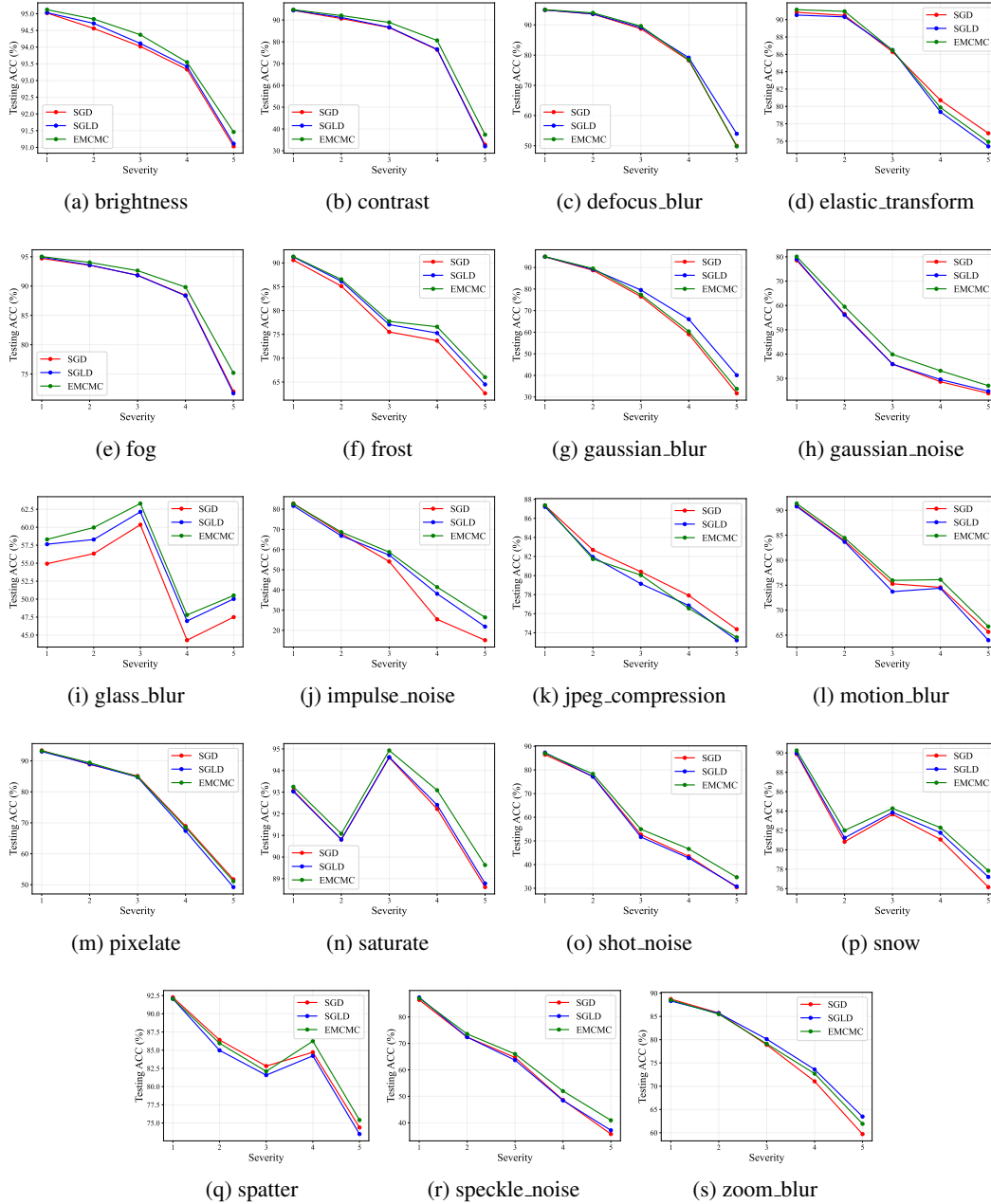


Figure 11: Classification accuracies under different severity levels on corrupted CIFAR. The results are shown per corruption type. Our method outperforms the compared baselines on most of corruption types, especially under high severity levels.